Evolution of photoluminescence as a function of the structural order or disorder in CaMoO4 nanopowders

A. P. A. Marques, F. V. Motta, E. R. Leite, P. S. Pizani, J. A. Varela et al.

Evolution of photoluminescence as a function of the structural order or disorder in CaMoO$_4$ nanopowders

A. P. A. Marques,[1,a] F. V. Motta,[1] E. R. Leite,[1] P. S. Pizani,[2] J. A. Varela,[3] E. Longo,[3] and D. M. A. de Melo[4]

[1]*LIEC-CMDMC, DQ, UFSCar, Via Washington Luiz, km 235, CEP 13565-905 São Carlos, SP, Brazil*
[2]*Laboratório de Semicondutores, DF, UFSCar, Via Washington Luiz, km 235, CEP 13565-905 São Carlos, SP, Brazil*
[3]*LIEC-CMDMC, IQ, UNESP, Rua Francisco Degni s/n, CEP 14800-900 Araraquara, SP, Brazil*
[4]*Laboratório de Análise Térmica e Materiais, DQ, UFRN, 59072-970, Natal, RN, Brazil*

CaMoO$_4$ nanopowders were prepared by the complex polymerization method. The materials were characterized by x-ray diffraction (XRD) and by Fourier transform infrared, Raman, and optical reflectance spectroscopies. The data revealed the presence of crystalline scheelite-type phase CaMoO$_4$ and the absence of additional phases. The surface morphology was monitored by high-resolution scanning electron microscopy (HR-SEM). The HR-SEM and XRD characterizations both revealed a tendency for the particle size to increase with rising treatment temperatures. The disordered nanopowders showed strong emission of photoluminescence, which dropped to minimal levels in the ordered nanopowders. These differences in the photoluminescence of disordered and ordered nanopowders were attributed to complex cluster vacancies. © *2008 American Institute of Physics*. [DOI: 10.1063/1.2968388]

I. INTRODUCTION

Molybdates with a scheelite-type crystalline structure (tetragonal symmetry C_{4h}^6), such as calcium molybdate (CaMoO$_4$), present excellent optical properties, which justify their widespread use as phosphors, laser materials, and scintillation detectors.[1,2] Because of their applications as a scintillating medium and in other electro-optical devices (i.e., solid-state laser and optical fibers), much interest has been focused on the investigation of materials with scheelite-type crystalline structures, aiming to gain a deeper understanding of the luminescent properties of molybdates.[3,4]

A variety of techniques is employed to obtain material similar to the CaMoO$_4$ (CMO) presented in this work, including the Czochralski method,[5] the combustion method,[6] and the solid-state reaction method.[7] Some methods involve high temperatures and long reaction times; however, the tendency for MoO$_3$ to vaporize at high temperatures can result in nonhomogeneous morphologies and compositions.[8]

The complex polymerization method (CPM) promotes morphological and compositional homogeneities because it involves synthesis at low temperatures, thereby, immobilizing the metal complexes in rigid organic polymeric networks. This reduces segregation of the metals, ensuring compositional homogeneity on the molecular scale.

Crystalline molybdates and tungstates with scheelite-type crystalline structures are technologically interesting materials for application in solid-state optoelectronic devices because of their strong natural green photoluminescence (PL) at room temperature. The PL spectra presented by these materials can often be decomposed into green, yellow, and red contributions. However, there are various controversial interpretations of molybdate and tungstate PL spectra, mainly in terms of their green contribution. Groenink and Blasse[9] and Korzhik and co-workers[10–12] concluded that green emission originates from the (WO$_3$+F) center. Sokolenko *et al.*[13] attributed green-red emission to WO$_3$ and $V_O^{..}$ oxygen-deficient complexes. Sinelnikov *et al.*[14] suggested that WO$_4$ tetrahedra, which become distorted upon the formation of oxygen vacancies are responsible for the green luminescence band. Moreover, several authors attribute the green PL component to defective sites with oxygen vacancies.[15–18] Our group recently demonstrated that the green PL component increases along with the structural order, and that when the structure is not completely ordered it displays intense visible PL at room temperature.[19–21]

Considering that the CPM is an efficient soft chemical method to prepare complex oxide materials and that there are controversial interpretations of the PL spectra of molybdate, this work reports on the preparation of ordered and disordered CaMoO$_4$ nanopowders by CPM and on their characterization. Various complementary characterization techniques were used, including x-ray diffraction (XRD), optical reflectance spectroscopy, Fourier transform infrared (FTIR) spectroscopy, and PL spectroscopy to obtain a clearer picture of the physics underlying the luminescence behavior of ordered and disordered CaMoO$_4$ scheelite structures. High-resolution scanning electron microscopy (HR-SEM) was used to detect the microstructure and surface morphology of the CaMoO$_4$ nanopowders.

II. EXPERIMENTAL PROCEDURE

The materials used in the preparation of CaMoO$_4$ nanopowders were molybdenum trioxide MoO$_3$ (Synth, 85%), CaCO$_3$ (Mallinckrodt, 99%), citric acid (H$_3$C$_6$H$_5$O$_7$) (Mallinckrodt 99%), and ethylene glycol (HOCH$_2$CH$_2$OH) (J. T. Baker, 99%). All the chemicals were used without further purification.

[a]Author to whom correspondence should be addressed. Electronic mail: apamarques@liec.ufscar.br.
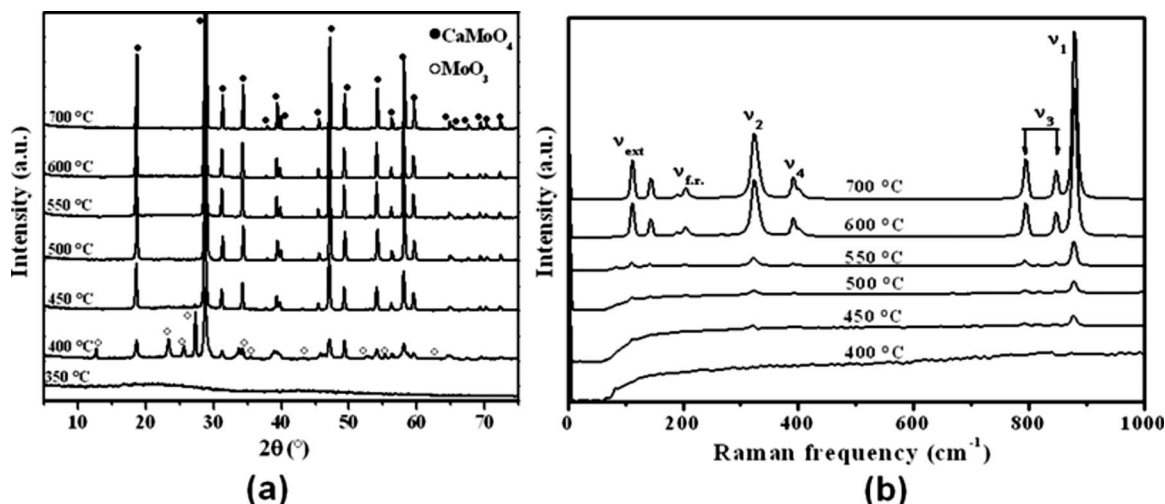
FIG. 1. Ordered and disordered CMO nanopowders: (a) XRD patterns of $CaMoO_4$ heat treated at 350, 400, 450, 500, 550, 600, and 700 °C, where (●) represents the $CaMoO_4$ phase and (○) represents the MoO_3 admixture phase, and (b) spontaneous Raman spectra of CMO heat treated at 400, 450, 500, 550, 600, and 700 °C.

In the CPM technique used here, the molybdenum citrate was first synthesized by dissolving MoO_3 molybdenum trioxide in an aqueous solution of citric acid under constant stirring at 60–80 °C to homogenize the solution. After homogenization, calcium carbonate was dissolved and added to the molybdenum citrate solution. The molar ratio of calcium to molybdenum cations was 1:1 and the molar ratio of citric acid to the sum of metals was 6:1. The complex was thoroughly stirred for several hours at 60–80 °C to produce a clear and homogeneous solution. After homogenization, ethylene glycol was added to promote polyesterification. The citric acid to ethylene glycol mass ratio was set at 60:40. With continued heating at 80–90 °C the viscosity of the solution increased, although it showed no visible phase separation.

Once the polymeric resin was obtained, the solution was heat treated at 350 °C for 2 h in a static oxidizing atmosphere, leading to its partial decomposition and forming an expanded resin consisting of partially pyrolyzed material. The resulting product was removed from the beaker and ground in a mortar. The powders were annealed in a static oxidizing atmosphere at 400, 450, 500, 550, 600, and 700 °C for 2 h at a heating rate of 5 °C/min.

CMO nanopowders were characterized by XRD using Cu $K\alpha$ radiation in order to determine the structural evolution and the unit cell volume of the nanopowders. The average crystallite diameter (D_{crys}) was determined by XRD, based on the (112) diffraction peak of the $CaMoO_4$ phase (2θ at around 28.8°), according to Scherrer's equation.[21–23] The microstructure and surface morphology of the CMO annealed between 400–700 °C were observed by HR-SEM, using a field emission (Supra 35 Gemini–Zeiss microscope).

The FTIR spectra were determined in the frequency range of 390–2000 cm^{-1} at room temperature, using an Equinox/55 (Bruker) spectrometer. The measurements were taken in transmittance mode. The optical reflectance of the powders was measured in the wavelength range of 200–800 nm, using an UV-visible-near infrared Cary 5G spectrophotometer. The Raman spectroscopy data were obtained at room temperature, using a RFS/100/S Bruker FT-Raman spectroscope with a spectral resolution of 4 cm^{-1} coupled to a Nd:YAG (yttrium aluminum garnet) laser, promoting an excitation light of 1064 nm in the frequency range of 100–1000 cm^{-1}.

The PL spectra of the CMO were collected with a U1000 Jobin-Yvon double monochromator coupled to a cooled GaAs photomultiplier and a conventional photon counting system. The 488.0 nm exciting wavelength of an argon ion laser was used. The maximum output power of the laser was 20 mW. All the measurements were taken at room temperature.

III. RESULTS AND DISCUSSION

The XRD patterns of the CMO annealed at 350 °C were disordered and no crystalline phases was observed [Fig. 1(a)]. $CaMoO_4$ scheelite-type crystalline phase and MoO_3 admixture phase were identified at 400 °C.[4,24–27] As the calcination temperature increased, the (021) diffraction peak, which is the maximum peak of the MoO_3 metastable phase (2θ at around 27.4°), disappeared and only the reflection peaks corresponding to $CaMoO_4$ crystalline phase remained. All the diffraction peaks were indexed according to the Joint Committee for Powder Diffraction Standard (JCPDS) database and indicated a scheelite-type tetragonal symmetry.[27]

The lattice parameters were calculated from the peak positions displayed in Fig. 1(a) using the least-squares refinement resource of the REDE93 software program. The lattice parameters **a** and **c** for CMO were also close to the values reported for bulk material (a=5.226 Å and c=11.43 Å).[27] The crystallite sizes showed a tendency to increase along with rising heat treatment temperature. Table I presents the mean crystallite sizes and the lattice parameters **a** and **c**.

Raman spectroscopy is an effective tool for studying the effects of structural order and disorder. For a perfect crystal, the first-order Raman phonon spectrum consists of narrow lines that correspond to Raman-allowed zone center (Γ-point) modes, which obey definite polarization selection

TABLE I. CaMoO₄ crystallite sizes and lattice constants.

Sample CMO treatment temperature (°C)	Crystallite sizes[a] (nm)	Lattice constants[b] (Å)	
		a	c
400	25 ± 1	5.220(1)	11.429(5)
450	36 ± 2	5.223(1)	11.441(6)
500	41 ± 2	5.217(0)	11.422(3)
550	47 ± 2	5.227(1)	11.430(6)
600	46 ± 2	5.226(0)	11.438(1)
700	53 ± 3	5.227(1)	11.436(4)

[a]Calculated using the (112) 100% diffraction peak.
[b]a=5.226 Å and c=11.43 Å (Ref. 27).

rules. In the case of disordered crystals, however, the following features are expected in the phonon spectrum: (i) a broadening of the first-order Raman lines; (ii) activation of forbidden Raman phonons; (iii) appearance of broad Raman bands reflecting the phonon density of states; (iv) frequency shifting of some peaks proportional to the concentration of the dopant element (i.e., one-phonon-like behavior); and (v) splitting of some peaks involving different elements that share the same lattice site (i.e., two-phonon-like behavior).[28]

According to Basiev *et al.*,[29] the primitive cell of CaMoO₄ includes two formulaic units, the [MoO₄]²⁻ ionic group with strong covalent Mo–O bonds (T_d symmetry) and the Ca²⁺ cations. Due to weak coupling between the [MoO₄]²⁻ ionic group and the Ca²⁺ cations, the vibrational modes observed in the spontaneous Raman spectra of CaMoO₄ scheelite crystals can be divided into two groups: internal and external modes. The internal vibrons correspond to the vibrations within the [MoO₄]²⁻ group with an immovable mass center. The external vibrons or lattice phonons correspond to the motion of the Ca²⁺ cations and the rigid molecular unit.

The scheelite primitive cell presents 26 different vibration modes: $\Gamma_{Td}=3A_g+5A_u+5B_g+3B_u+5E_g+5E_u$, but only A_g, B_g, and E_g are Raman active. The spontaneous Raman spectra with the assignments of the Raman-active vibration modes of the CMO nanopowders are presented in Fig. 1(b) and detailed in Table II.

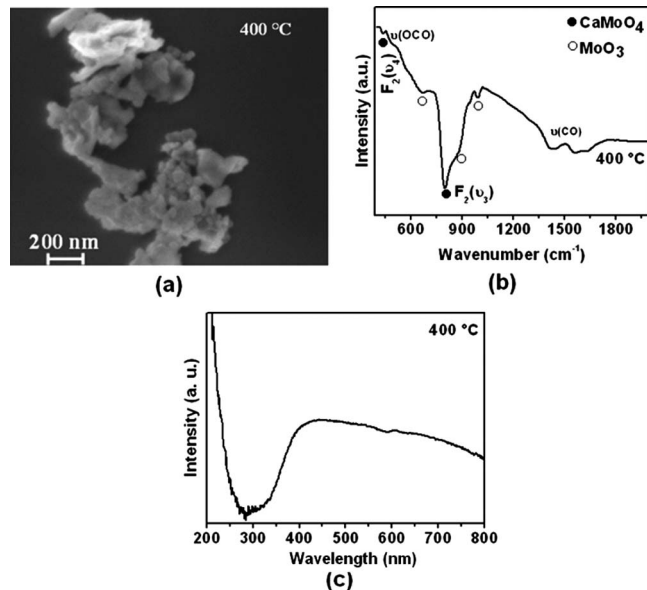The Raman spectra all showed sharp well-resolved

FIG. 2. Disordered CaMoO₄ nanopowders heat treated at 400 °C: (a) HR-SEM micrograph, (b) FTIR absorption spectra, and (c) reflectivity spectra.

peaks (external and internal modes) for the CMO treated at 600 and 700 °C, indicating that the synthesized powders were highly crystallized with long- and short-range orders and with few defects (such as O vacancies). In the CMO treated at 450–550 °C, the main peaks were present but displayed only internal modes, which is indicative of the beginning of long-range order. This fact indicates that the material's structure was partially disordered. The CMO annealed at 400 °C displayed no sharp peaks corresponding to the CaMoO₄ phase, indicating that the material was totally disordered.

The HR-SEM micrograph of CMO heat treated at 400 °C presented particle agglomerates with undefined grain contours [Fig. 2(a)]. Increasing the treatment temperature resulted in a tendency for defined contours and larger grain sizes [Fig. 3(a)]. Micrographs of CMO annealed at 500, 600, and 700 °C revealed small and large particles and indicated that small particles coalesced, forming large particles. Both HR-SEM and XRD revealed the tendency for the grain size to increase with rising heat treatment temperature.

TABLE II. CaMoO₄ vibrational modes and Raman peaks.

Vibrational mode and symmetry		Raman peaks (cm⁻¹)			
Isolated tetrahedrons T_d	Lattice mode symmetry C_{4h}^6	CMO[a]			CMO[b]
		450 °C	500 °C	550–700 °C	
$\nu_1(2A_1)$	A_g	878	878	878	878
$\nu_3(2F_2)$	B_g	846	847	847	844
	E_g	791	793	794	797
$\nu_4(2F_2)$	E_g		403	402	401
	B_g	392	391	391	393
$\nu_2(2E)$	B_g, A_g	323	323	323	333
$\nu_{f.r.}(2F_1)$ free rotation	E_g		204	204	205
ν_{ext} external modes MoO₄²⁻ and Ca²⁺ motions	B_g		143	143	
	E_g		112	112	
	B_g, E_g			86	

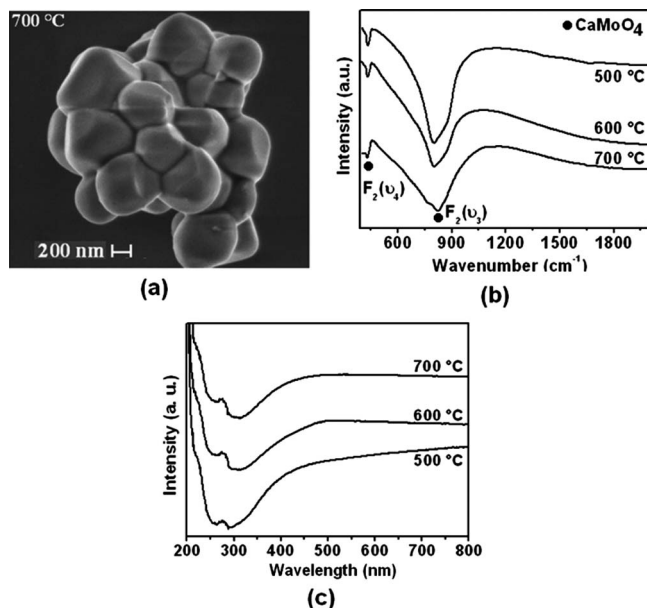[a]The present work.
[b]Reference 41.

FIG. 3. Ordered $CaMoO_4$ nanopowders heat treated at 500, 600, and 700 °C: (a) HR-SEM micrograph, (b) FTIR absorption spectra, and (c) reflectivity spectra.

TABLE III. $CaMoO_4$ optical energy band gap (E_g) data.

CMO samples	E_g (eV)
400 °C	5.09
500 °C	4.87
600 °C	5.18
700 °C	5.16

The optical energy band gap (E_g) for CMO was estimated by plotting $(\alpha h \nu)^2$ as a function of $h\nu$, as described by Tauc and Menth's law.[32] The α value obtained for CMO was higher than 10^4. According to Sian and Reddy[33] α values above 10^4 confirm the existence of direct band gaps. Zhang *et al.*[34] demonstrated that the valence and conduction bands near the band gap are dominated by molecular orbitals associated with the MoO_4^{-x} ions, where $x \approx 2$, and also that $CaMoO_4$ has a direct band gap. Based on experimental data, the E_g values calculated for CMO ranged from 4.87 to 5.18 eV, which are similar to the values reported by Ryu *et al.*[4,35] (see Table III).

The three different charge states occurring in oxygen vacancies in molybdenum are $[MoO_3 \cdot V_O^X]$, $[MoO_3 \cdot V_O^\cdot]$, and $[MoO_3 \cdot V_O^{\cdot\cdot}]$ complex states. The $[MoO_3 \cdot V_O^X]$ complex state presented two paired electrons $\uparrow\downarrow$ and was neutral relative to the lattice. The singly ionized $[\overline{Mo}O_3 \cdot V_O^\cdot]$ complex state had one unpaired electron $\uparrow$ and the $[MoO_3 \cdot V_O^{\cdot\cdot}]$ complex state did not trap any electrons and was doubly positively charged with respect to the lattice. We speculate that these oxygen vacancies induced new energy in the band gap and were attributable to the molybdenum-oxygen complex vacancy centers.

Figures 4(a)–4(e) illustrate the PL spectra recorded at room temperature for the CMO nanopowders heat treated at 400–700 °C. The profile of the emission band is typical of a multiphonon process, i.e., a system in which relaxation occurs by several paths, involving the participation of numerous states within the band gap of the material. This behavior is related to the structural disorder of CMO and indicates the presence of additional electronic levels in the forbidden band gap of the material.

The characteristic PL emission showed broad and intense bands between ~470 and 820 nm, mostly for the disordered nanopowders annealed at 400–500 °C and centered at 577 nm (2.15 eV). The intensity of the PL of disordered nanopowders at the subsequent annealing temperatures decreased and the center shifted to around 45 nm in CMO annealed at 550 °C (532 nm, 2.33 eV). The PL emission of structurally ordered CMO (600–700 °C) practically disappeared.

The difference between the excitation and the emission maximum (Stokes shift) may denote the strength of the electron-phonon interaction. Note that the Stokes shift decreased gradually in the disordered CMO and considerably in the ordered CMO, indicating dependence on the degree of disorder in the lattice and on the electron-phonon interaction. This rearrangement of the lattice in disordered CMO annealed at 400–550 °C was not detected by long-range XRD measurements [Fig. 1(a)]. However, the experimental UV

The representation of tetrahedral symmetry is $\Gamma_{Td} = A_1(\nu_1) + E(\nu_2) + F_2(\nu_3) + F_2(\nu_4)$, but only the $F_2(\nu_3, \nu_4)$ modes are IR active, and the vibrations correspond to antisymmetric stretching and bending modes, respectively. The FTIR spectra of CMO annealed at 400 °C presented bands ascribed to carbonate groups. In line with the report of Nakamoto,[30] $\nu(CO)$ stretching occurred at 2375 –1100 cm^{-1} and $\nu(OCO)$ stretching took place at 1100 –550 cm^{-1}, indicating that undecomposed organic ligands were still present in these powders [Fig. 2(b)]. Bands corresponding to MoO_3 and $CaMoO_4$ phases were also present in CMO heat treated at 400 °C. The stretching at around 670, 880, and 990 cm^{-1} corresponded to the MoO_3 phase and at around 438 and 800 cm^{-1} to the $CaMoO_4$ phase.

Figure 3(b) depicts the spectra of ordered CMO 500–700 °C, showing an absorption band corresponding to the Mo–O stretching vibration in MoO_4^{2-} tetrahedra from 800 to 820 cm^{-1} for the $F_2(\nu_3)$ vibrations and at around 430 cm^{-1} for the $F_2(\nu_4)$ vibrations.[30] A MoO_3 admixture phase and organic ligands were decomposed as the treatment temperature increased, which favored structural order and led to more well-defined Mo–O bands [Figs. 2(b) and 3(b)]. These observations confirm the XRD and Raman data, which indicated an increase in the crystalline order with rising treatment temperature (Fig. 1).

Reflectivity spectra of CMO heat treated at 500–700 °C presented a band at 276 nm (4.49 eV), which was attributed to electronic transitions within the MoO_4^{2-} complex [Fig. 3(c)].[31] The disordered CMO did not present the band corresponding to electronic transitions within the MoO_4^{2-} complex [Fig. 2(c)]. Similar to Spassky *et al.*,[31] our CMO reflectivity spectra did not show a band corresponding to the creation of the excitonic state in cation A^{2+} (A=Ca), which usually occurs at around 344 nm (3.60 eV).
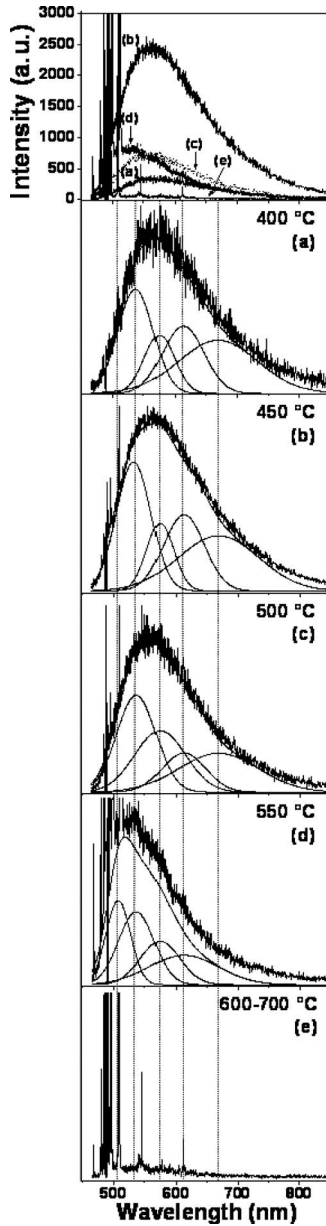
FIG. 4. Room temperature PL spectra of CaMoO$_4$ nanopowders excited with the 488 nm line of an argon ion laser and heat treated for 2 h at (a) 400 °C, (b) 450 °C, (c) 500 °C, (d) 550 °C, and (e) 600–700 °C, and their respective PL components in the bluish-green, green, yellow, orange, and red regions.

TABLE IV. Fitting parameters of the Gaussian peaks for PL obtained with excitation wavelength at 488 nm (T is the temperature of heat annealing, BGC is the blue-green component of PL, GC is the green component of PL, YC is the yellow component of PL, OC is the orange component of PL, and RC is the red component of PL).

T (°C)	BGC (%)[a]	GC (%)[a]	YC (%)[a]	OC (%)[a]	RC (%)[a]
400	0	29	14	22	35
450	0	32	13	23	32
500	0	32	26	15	27
550	25	31	20	24	0

[a]Obtained by dividing the area of each of the decomposed PL curves by the total PL area.

To gain a better understanding of the PL properties and their dependence on the structural order-disorder of the lattice, the PL curves were analyzed using a deconvolution PICKFIT.[38] The PL curves were well fitted with five Gaussian PL components consisted of five PL components, herein called bluish-green component (maximum at 508 nm), green component (maximum at 537 nm), yellow component (maximum at 575 nm), orange component (maximum at 613 nm), and red component (maximum at 669 nm), in allusion to the region where the maximum of the component appears. Each color represents a different type of electronic transition and is linked to a specific structural arrangement. The features extracted from deconvolution curves and the area under the curve of the respective transitions are listed in Table IV and shown in Figs. 4(b)–4(d).

The structure of the CMO nanopowders became more ordered as the treatment temperature increased, favoring green light emission (smaller wavelength) with higher energies (Fig. 4). Molybdenum, which is the lattice former, ideally tends to bond with four oxygen atoms, but before it reaches this ideal configuration there are various coordination numbers for Mo in the structure. Before crystallization, the structure is a mixture of MoO$_x$ complex clusters (x =mostly 3 and 4) intercalated with Ca atoms. The higher the annealing temperature, the more frequent the [MoO$_4$] complex clusters and the more ordered the structure. In PL spectra, the yellow, orange, and red area bands decrease and the green area bands increase with the heat treatment, since yellow-orange-red emission is linked to the disordered structure and green emission is linked to the ordered structure.[20] Before donor excitation in disordered structure, a hole is created in the acceptor and an electron in the donor, according to the following equations in which Kröger–Vink notation is used for complex clusters:

and PL measurements indicated that significant changes occurred in the gap states as the system became ordered [Figs. 2(c) and 3(c)].

The luminescence process is generally described by a Gaussian line broadening mechanism, whereby the intensity of luminescence can be expressed in terms of a Gaussian (amplitude version) line-shape function and can be written as follows:

$$I(h\nu) = I_0 + \sum_{i=1}^{n} A_i \exp\left[-\frac{(h\nu) - E_{0i}}{2\sigma_i^2}\right], \quad (1)$$

where $h\nu$ is the energy of the radiation emitted, I_0 is the offset, A_i is the amplitude, E_{0i} is the energy at which the intensity is at its maximum, and σ_i is the standard derivation full width at half maximum and its component or transition.[36,37]

$$[\text{MoO}_4]^x + [\text{MoO}_3 \cdot V_O^x] \rightarrow [\text{MoO}_4]' + (\text{MoO}_3 \cdot V_O), \quad (2)$$

$$[\text{MoO}_4]^x + [\text{MoO}_3 \cdot V_O] \rightarrow [\text{MoO}_4]' + (\text{MoO}_3 \cdot V_O^{\cdot}), \quad (3)$$

where [MoO$_4$]′ are donors, [MoO$_3 \cdot V_O$] are donors/acceptors, and [MoO$_3 \cdot V_O^{\cdot\cdot}$] are acceptors. In the complex, the [MoO$_4$]′ clusters act as electron donors while the vacancy complex [MoO$_3 \cdot V_O$] tends to trap electrons and/or holes and [MoO$_3 \cdot V_O^{\cdot\cdot}$] acts as an electron trap.

Equations (2) and (3) suggest that the oxygen-vacancy-trapped electron in the valence band is a requirement for the transition of a valence-band hole in the conduction band in disordered structure. This means that most of the electrons around oxygen vacancies are released and, therefore, such oxygen vacancy complex sites are relatively positively charged. Moreover, oxygen vacancies tend to trap photogenerated electrons. The charge transfer that takes place as proposed in Eqs. (2) and (3) creates electrons and hole polarons that can be designed as bipolarons. After photon excitation, the recombination and decay process follow the many valid hypotheses presented in the literature.[39,40]

Therefore, the present work shows that MoO_x complex clusters already existing in the ground state facilitate the emission process that leads to PL, i.e., radiative recombination. Thus, the ordered-disordered CMO nanopowders intrinsically possess the necessary condition for creating PL at room temperature.

IV. CONCLUSION

A simple method, the CPM, is used to prepare $CaMoO_4$ nanopowders with the advantage of requiring lower temperatures, shorter processing times, and involving lower costs. The $CaMoO_4$ scheelite-type crystalline phase and the MoO_3 admixture phase were identified at 400 °C. At a higher treatment temperature, the MoO_3 phase disappeared and the crystalline phase was identified without additional phases. HR-SEM revealed a tendency for well-defined grain contours and larger grain sizes as the treatment temperature increased. The inherent defects were linked to structural disorder already existing in the ground state, facilitating the emission process leading to PL, i.e., radioactive recombination. This work showed that the PL intensity and the band emission energy photons depend on the structural order-disorder and therefore on the thermal treatment history. The optical properties suggest that the $CaMoO_4$ obtained by CPM is a highly promising candidate for PL applications.

ACKNOWLEDGMENTS

[1] N. Klassen, S. Shmurak, B. Red'kin, B. Ille, M. Lebeau, P. Lecoq, and M. Schneegans, Nucl. Instrum. Methods Phys. Res. A **486**, 431 (2002).
[2] F. A. Danevich, A. S. Georgadze, V. V. Kobychev, B. N. Kropivyansky, V. N. Kuts, A. S. Nikolaiko, V. I. Tretyak, and Y. Zdesenko, Phys. Lett. B **344**, 72 (1995).
[3] F. A. Kroger, *Some Aspects of the Luminescence of Solids* (Elsevier, Amsterdam, 1948).
[4] J. H. Ryu, J. W. Yoon, C. S. Lim, W. C. Oh, and K. B. Shim, J. Alloys Compd. **390**, 245 (2005).
[5] V. B. Mikhailik, H. Kraus, D. Wahl, and M. S. Mykhaylyk, Phys. Status Solidi B **242**, R17 (2005).
[6] P. Yang, G. Q. Yao, and J. H. Lin, Inorg. Chem. Commun. **7**, 389 (2004).
[7] Y. S. Hu, W. D. Zhuang, and H. Q. Ye, J. Rare Earths **22**, 821 (2004).
[8] W. S. Cho, M. Yashima, M. Kakihana, A. Kudo, T. Sakata, and M. Yoshimura, J. Am. Ceram. Soc. **80**, 765 (1997).
[9] J. A. Groenink and G. Blasse, J. Solid State Chem. **32**, 9 (1980).
[10] A. A. Annenkov, M. V. Korzhik, and P. Lecoq, Nucl. Instrum. Methods Phys. Res. A **490**, 30 (2002).
[11] P. Lecoq, I. Dafinei, E. Auffray, M. Schneegans, M. V. Korzhik, O. V. Missevitch, V. B. Pavlenko, A. A. Fedorov, A. N. Annenkov, V. L. Kostylev, and V. D. Ligun, Nucl. Instrum. Methods Phys. Res. A **365**, 291 (1995).
[12] M. V. Korzhik, V. B. Pavlenko, T. N. Timoschenko, V. A. Katchanov, A. V. Singovskii, A. N. Annenkov, V. A. Ligun, I. M. Solskii, and J. P. Peigneux, Phys. Status Solidi A **154**, 779 (1996).
[13] E. V. Sokolenko, V. M. Zhukovskii, E. S. Buyanova, and Y. A. Krasnobaev, Inorg. Mater. **34**, 499 (1998).
[14] B. M. Sinelnikov, E. V. Sokolenko, and V. Y. Zvekov, Inorg. Mater. **32**, 999 (1996).
[15] T. L. Chen, X. M. Li, K. S. Wan, W. L. Zhu, and G. Pezzotti, Appl. Phys. Lett. **87**, 181914 (2005).
[16] S. Myhajlenko, A. Bell, F. Ponce, J. L. Edwards, Y. Wei, B. Craigo, D. Convey, H. Li, R. Liu, and J. Kulik, J. Appl. Phys. **97**, 014101 (2005).
[17] T. Hara, Mater. Chem. Phys. **91**, 243 (2005).
[18] Y. H. Chen, C. S. Shi, and G. Q. Hu, J. Appl. Phys. **87**, 1503 (2000).
[19] M. Anicete-Santos, F. C. Picon, M. T. Escote, E. R. Leite, P. S. Pizani, J. A. Varela, and E. Longo, Appl. Phys. Lett. **88**, 211913 (2006).
[20] V. M. Longo, E. Orhan, L. S. Cavalcante, S. L. Porto, J. W. M. Espinosa, J. A. Varela, and E. Longo, Chem. Phys. **334**, 180 (2007).
[21] A. P. A. Marques, D. M. A. de Melo, E. Longo, C. A. Paskocimas, P. S. Pizani, and E. R. Leite, J. Solid State Chem. **178**, 2346 (2005).
[22] C. S. M. G. Norton, *X-Ray Diffraction: A Practical Approach* (Plenum, New York, 1998).
[23] A. P. A. Marques, D. M. A. Melo, C. A. Paskocimas, P. S. Pizani, M. R. Joya, E. R. Leite, and E. Longo, J. Solid State Chem. **179**, 658 (2006).
[24] V. Nassif and R. E. Carbonio, J. Solid State Chem. **146**, 266 (1999).
[25] C. T. Xia, V. M. Fuenzalida, and R. A. Zarate, J. Alloys Compd. **316**, 250 (2001).
[26] V. Thangadurai, C. Knittlmayer, and W. Weppner, Mater. Sci. Eng., B **106**, 228 (2004).
[27] JCPDS Card No. 29-0193 (unpublished).
[28] M. R. Moura, A. P. Ayala, I. Guedes, M. Grimsditch, C. K. Loong, and L. A. Boatner, J. Appl. Phys. **95**, 1148 (2004).
[29] T. T. Basiev, A. A. Sobol, Y. K. Voronko, and P. G. Zverev, Opt. Mater. **15**, 205 (2000).
[30] K. Nakamoto, *Infrared and Raman Spectra of Inorganic and Coordination Compounds* (Wiley, New York, 1986).
[31] D. A. Spassky, S. N. Ivanov, V. N. Kolobanov, V. V. Mikhailin, V. N. Zemskov, B. I. Zadneprovski, and L. I. Potkin, Radiat. Meas. **38**, 607 (2004).
[32] D. L. Wood and J. Tauc, Phys. Rev. B **5**, 3144 (1972).
[33] T. S. Sian and G. B. Reddy, Sol. Energy Mater. Sol. Cells **82**, 375 (2004).
[34] Y. Zhang, N. A. W. Holzwarth, and R. T. Williams, Phys. Rev. B **57**, 12738 (1998).
[35] J. H. Ryu, B. G. Choi, J. W. Yoon, K. B. Shim, K. Machi, and K. Hamada, J. Lumin. **124**, 67 (2007).
[36] R. A. Street, Adv. Phys. **25**, 397 (1976).
[37] P. R. Bevington, *Data Reduction and Error Analysis for the Physical Sciences* (McGraw-Hill, New York, 1969).
[38] T. Ding, W. T. Zheng, H. W. Tian, J. F. Zang, Z. D. Zhao, S. S. Yu, X. T. Li, F. L. Meng, Y. M. Wang, and X. G. Kong, Solid State Commun. **132**, 815 (2004).
[39] R. Leonelli and J. L. Brebner, Solid State Commun. **54**, 505 (1985).
[40] R. I. Eglitis, E. A. Kotomin, and G. Borstel, Eur. Phys. J. B **27**, 483 (2002).
[41] S. P. S. Porto and J. F. Scott, Phys. Rev. **157**, 716 (1967).